Supplement of Geosci. Model Dev., 14, 961–984, 2021
https://doi.org/10.5194/gmd-14-961-2021-supplement

Geoscientific Model Development
Open Access
EGU

Supplement of

The Vertical City Weather Generator (VCWG v1.3.2)

Mohsen Moradi et al.

Correspondence to: Amir A. Aliabadi (aliabadi@uoguelph.ca)

S1 Model Exploration and Comparison with Limited UHI Observations

The VCWG performance is assessed by evaluating the model performance as a function of the urban configurations (λ_{p} [-], λ_{f} [-], LAD [$\mathrm{m^2 m^{-3}}$]), building energy configuration (building type, thermal efficiency, coefficient of performance, location of building waste heat release), radiation configuration (canyon aspect ratio and axis angle), different seasons, and different climate zones. Except for the analysis of different seasons and climate zones, all explorations are performed by VCWG simulations of the urban micro-climate in Basel, Switzerland, for two weeks starting 15 June 2002, concurrent with the BUBBLE campaign. For analysis of different seasons, simulation results of VCWG are provided for Vancouver for an entire year in a period in early 2000s. For different climate zones, VCWG simulations are conducted for other cities for a two-week period during the summer season. More details on the explorations are provided in the subsequent sections. Such analyses will provide more information on spatio-temporal variation of the atmospheric meteorological variables and reveal the complexity of urban micro-climate modeling. Additionally, the potentials and limitations of VCWG will be discussed.

S1.1 Urban Plan and Frontal Area Densities

In urban canopy modeling, two parameters often used to describe building and canyon geometries are plan area density λ_{p} [-], which is the ratio of the total plan area of the buildings to the total urban flat-earth surface area, and the frontal area density λ_{f} [-], which is the ratio of the total frontal area (facing wind) to the total urban flat-earth surface area. An urban area can be characterized with different types of land use, where each type may have different plan and frontal area densities varying from high values in industrial and commercial districts to low values associated with the land used for public transportation (Wong et al., 2010). Most development in an urban area could be associated with changing λ_{p} [-] and λ_{f} [-], which can alter the local climate in different ways such as air and surface temperatures, building energy consumption, and thermal and wind comfort levels (Coutts et al., 2007; Emmanuel and Steemers, 2018).

Two case studies λ_{p}=0.46 and 0.54 [-] (associated with canyon widths of 25 and 18.2 m) are explored to assess the model and see how the urban micro-climate changes when the plan area density decreases. Here, except for canyon width, all other model input parameters are kept the same as the evaluation simulations. Figure S1 shows typical nighttime and daytime profiles of potential temperature, horizontal wind speed, specific humidity, and turbulent kinetic energy in the urban area associated with model simulations for two weeks corresponding to the BUBBLE field campaign. In this case, higher λ_{p} [-] is associated with more shading and therefore lower potential temperatures during the day. During the nighttime, the temperature difference between the cases is not as much as the daytime, however, still slightly higher temperatures can be obtained when plan area density is higher. Additionally, more urban surfaces by higher λ_{p} [-] impose more drag and consequently reduce wind speed and turbulent kinetic energy during both daytime and nighttime, which can also be depicted in Fig. S1. No change in specific humidity is noted in this exploration.

Further investigations are performed for different frontal area densities λ_{f}= 0.37 and 0.51 [-] (associated with building heights 14.6 and 20 m) by model simulations for two weeks associated with the BUBBLE field campaign. Here, except for building height, all other model input parameters are kept the same as the evaluation simulations. At first glance, the cities with high-rise buildings are supposed to release more heat into the outdoor environment due to greater urban surfaces, but tall buildings can provide solar shading during the daytime and decrease the temperature of the surfaces. As shown in Fig. S2, an increase in λ_{f} [-] reduces potential temperature in the urban area during the day. However, due to the lack of shortwave radiation over nighttime and that urban surfaces are the main source of heat that can be released into the atmosphere, higher λ_{f} [-] results in higher potential temperatures at nighttime because of longwave radiation trapping. Moreover, increasing frontal area density tends to increase surface roughness and consequently slow down wind speed and reduce the turbulent kinetic energy within the canyon during both daytime and nighttime, which can also be depicted in Fig. S2. No change in specific humidity is noted in this exploration. Note that skin drag is mostly related to roof level drag, which is less in magnitude compared to form drag caused by the building walls. This hypothesis can be confirmed using this exploration study. When λ_p is changed, it is noticed that wind speed profiles respond to a lesser extent compared to when λ_f is changed. The VCWG results are also consistent with previous studies in the literature (Coutts et al., 2007; Zajic et al., 2011; Santiago et al., 2014). The findings reported here highlight the careful considerations that need to be accounted for by city planners.

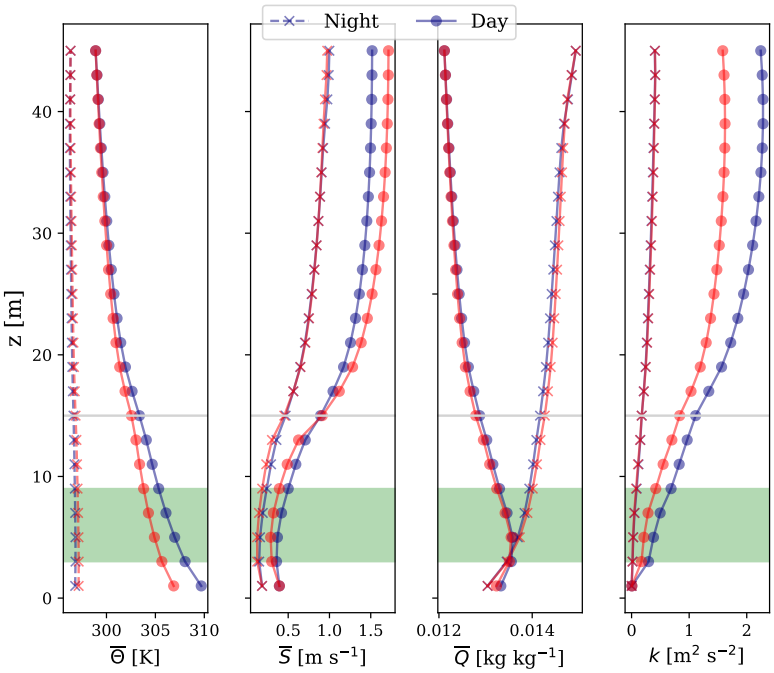

Figure S1. Effect of plan area density λ_p [-] on the profiles of potential temperature, horizontal wind speed, specific humidity, and turbulent kinetic energy during nighttime (averaged from 0000 to 0400 LST) and daytime (averaged from 1200 to 1600 LST); red: λ_p=0.54 [-], blue: λ_p=0.46 [-]; tree crown with non-zero LAD [m^2m^{-3}] shown in shaded green; building height shown with grey line; times in Local Standard Time (LST).

S1.2 Leaf Area Density

Urban trees interact with the other urban elements by providing shade to reduce the temperature of surfaces, removing the stored heat in the canyon substantially, and induce drag to reduce wind speed (Loughner et al., 2012; Krayenhoff et al., 2015; Redon et al., 2017). The capability of VCWG to take into account these effects is assessed by investigating two case studies with LAD [m^2m^{-3}] representing trees with canyon-average foliage densities of 0.1 and 0.2 m^2m^{-3}, respectively, by model simulations for two weeks associated with the BUBBLE field campaign. Here, except for LAD [m^2m^{-3}], all other model input parameters are kept the same as the evaluation simulations. The result is shown in Fig. S3. The cooling effect of the trees is evident when the average LAD [m^2m^{-3}] of tree foliage increases, resulting in a decrease of potential temperature within the canyon, particularly during the day when the shading effect of trees lowers the surface temperatures and the evapotranspiration of trees lowers the air temperature. Such effects not only can improve thermal comfort at the pedestrian level, but also can reduce the building energy consumption in the summertime (Souch and Souch, 1993; Akbari et al., 2001). On the other hand, the urban trees are thought to be a sink of momentum and kinetic energy by exerting drag and damping the flow fluctuations (Giometto et al., 2017; Yuan et al., 2017). This effect can also be modeled by VCWG, which predicts slightly lower level of wind speed within the canyon with increasing LAD [m^2m^{-3}]. Increasing LAD [m^2m^{-3}] reduces the turbulent kinetic energy, possibly due to the combined effects of reducing wind speed, LAD [m^2m^{-3}], and the drag coefficient for tree foliage C_{DV} [-], influencing the wake production term S_{wake} [m^2s^{-3}] (Krayenhoff, 2014). Increasing LAD [m^2m^{-3}], however, results in higher levels of specific humidity due to higher evapotranspiration of trees during daytime. The analysis obtained from this exploration is in reasonable agreement with previous works (Souch and Souch, 1993; Loughner et al., 2012; Giometto et al.,

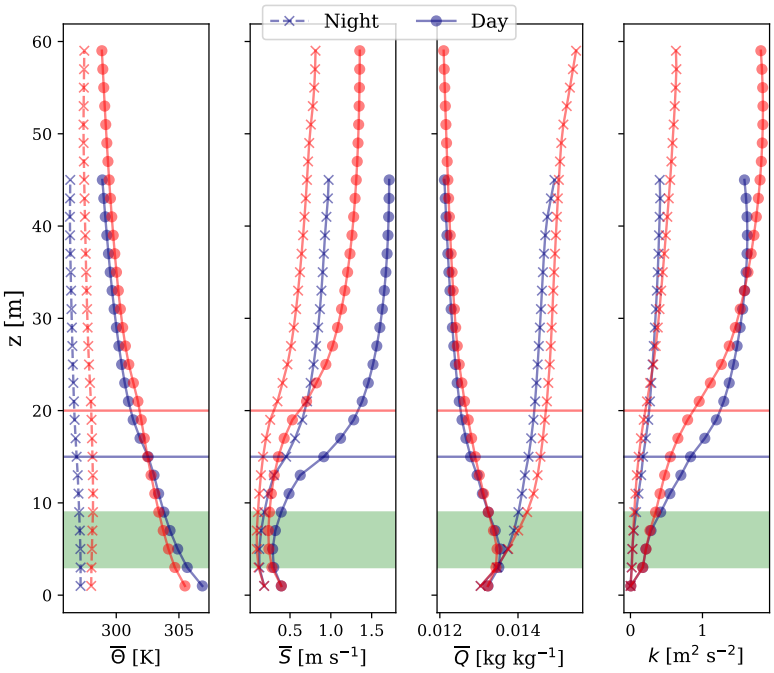

Figure S2. Effect of frontal area density λ_f [-] on the profiles of potential temperature, horizontal wind speed, specific humidity, and turbulent kinetic energy during nighttime (averaged from 0000 to 0400 LST) and daytime (averaged from 1200 to 1600 LST); red: λ_f=0.51 [-], blue: λ_f=0.37 [-]; tree crown with non-zero LAD [m^{2}m^{-3}] shown in shaded green; building heights shown with red and blue lines; times in Local Standard Time (LST).

2017; Yuan et al., 2017). Trees are recognized to be essential urban elements to moderate extreme wind speeds and heat waves, particularly during the warm season.

S1.3 Building Energy Configuration

The building energy model within VCWG is explored by VCWG simulations under different building types, cooling system Coefficient Of Performance (COP) [-], heating system thermal efficiency η_{heat} [-], and location of the release of building waste heat F_{st} [-]. Two building types are considered, the mid-rise apartment and a hospital, with specifications provided in Table 1. It can be noted that the infiltration rate, ventilation rate, volumetric flow for water heating, and waste heat fluxes associated with gas combustion, electricity consumption, and lighting for a hospital are substantially greater than those for a mid-rise apartment. Note that construction material properties are also different among different building types, which are specified in VCWG schedules. Two sets of COP [-] and η_{heat} [-] are considered for a mid-rise apartment. For an energy-efficient building default values COP=3.13 [-] and η_{heat}=0.8 [-] are used, while for a low-energy-efficient building values COP=1 [-] and η_{heat}=0.4 [-] are used. Note that these values for a low-energy efficient building are below permitted building code values in the U.S., but these values are chosen to amplify the effects on urban climate variables predicted by VCWG for clarity. For the location of the release of building waste heat three conditions are assumed: all waste heat is released at street level (F_{st}=1); half of waste heat is released at street level (F_{st}=0.5); and all waste heat is released at roof level (F_{st}=0). In these simulations, except for building type, COP [-], η_{heat} [-], and F_{st} [-], all other model input parameters are kept the same as the evaluation simulations.

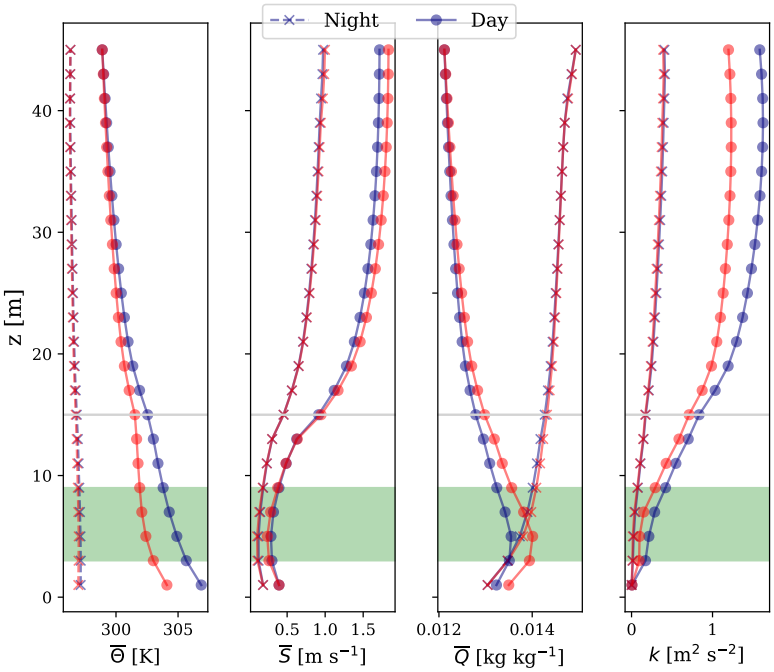

Figure S3. Effect of leaf area density profiles LAD [m^2m^{-3}] on the profiles of potential temperature, horizontal wind speed, specific humidity, and turbulent kinetic energy during nighttime (averaged from 0000 to 0400 LST) and daytime (averaged from 1200 to 1600 LST); red: LAD=0.2 m^2m^{-3}, blue: LAD=0.1 m^2m^{-3}; tree crown with non-zero LAD [m^2m^{-3}] shown in shaded green; building height shown with grey line; times in Local Standard Time (LST).

Table 1. Specifications of the building energy configuration for two building types; values extracted from the Urban Weather Generator (UWG) model (Bueno et al., 2012); the infiltration is expressed as Air Changes per Hour (ACH [-]).

Building type → Building specification ↓	Mid-rise apartment	Hospital
COP [-]	3.13	5.2
η_{heat} [-]	0.8	0.8
Infiltration (ACH [-])	0.64	0.22
Ventilation [$Ls^{-1}m^{-2}$]	0.45	1.8
Average waste heat flux from gas combustion [Wm^{-2}]	0	13
Average waste heat flux from electricity consumption [Wm^{-2}]	5	17
Average waste heat flux from lighting [Wm^{-2}]	5	22

Figure S4 shows the effect of building type on hourly mean and standard deviation of cooling/heating waste heat, dehumidification waste heat, gas combustion waste heat, water heating waste heat, and UHI [K] calculated for model simulations for two weeks. The waste heat fluxes are reported per unit building footprint area. It can be noted that the building energy system operates under heating mode for a few hours before sunrise, while it runs under cooling mode for the majority of daytime period. It can be noted that a hospital results in higher values of waste heats and UHI [K], so the potential impact of an energy-intensive hospital on the urban climate may be higher than a mid-rise apartment.

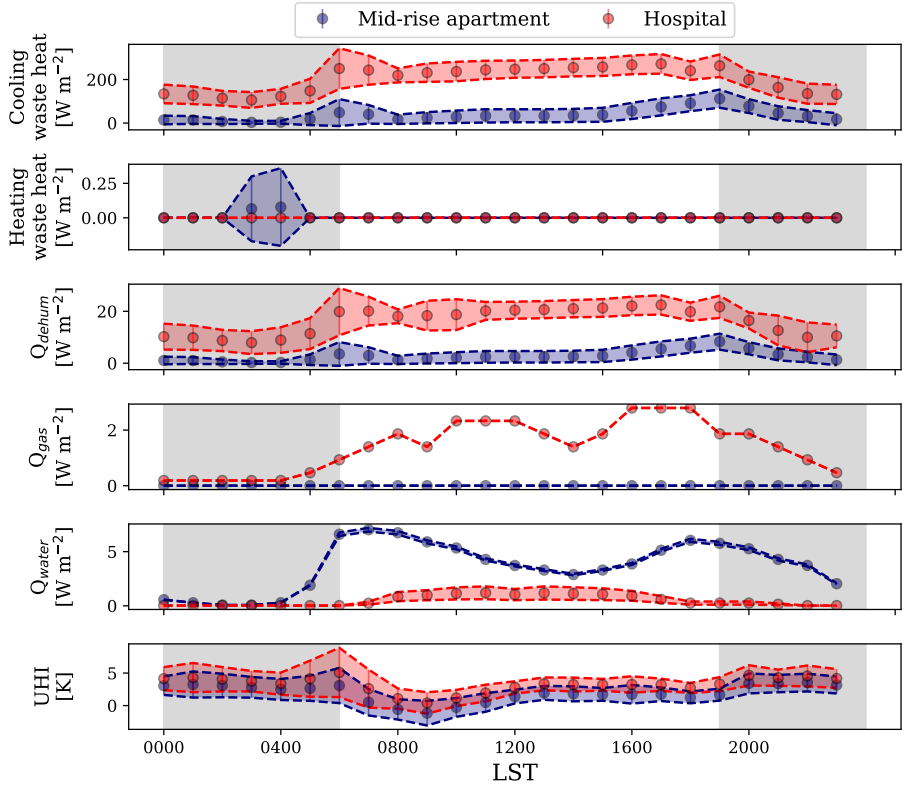

Figure S4. Effect of building type on cooling/heating waste heat, dehumidification waste heat, gas combustion waste heat, water heating waste heat, and UHI [K]; diurnal variation of mean and standard variation (band) are shown using data obtained over a two-week period; nighttime is shown with shaded regions; times in Local Standard Time (LST).

Figure S5 shows the effect of COP [-] and η_{heat} [-] on hourly mean and standard deviation of waste heats and UHI [K] calculated for model simulations for two weeks. It can be noted that lower COP [-] and η_{heat} [-] result in higher values of waste heats and slightly higher UHI [K], so the potential impact of an energy-intensive building on the urban climate may be higher than an energy-efficient building. Most particularly, it can be noted that lower heating system thermal efficiency results in greater waste heat flux for water heating.

Figure S6 shows the effect of F_{st} [-] on hourly mean and standard deviation of UHI [K] calculated for model simulations for two weeks. The figure considers cases where all waste heat is released at the street level (F_{st}=1), half of waste heat is released at street level and the other half of waste heat is released at roof level (F_{st}=0.5), and all waste heat is released at roof level (F_{st}=0). According to this analysis, on average, the UHI [K] value for the case with F_{st}=1, is higher by 1 K than the case with F_{st}=0. This can be attributed to a more effective mechanism to diffuse the waste heat upward due to higher wind

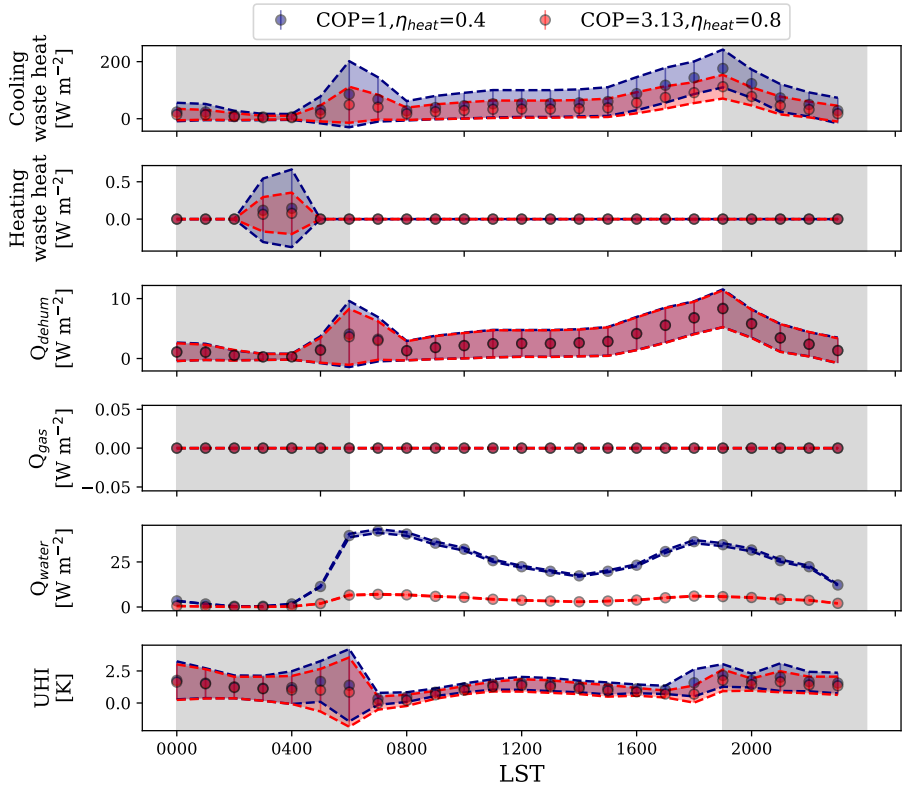

Figure S5. Effect of building cooling system Coefficient Of Performance (COP [-]) and heating system thermal efficiency (η_{heat} [-]) on cooling/heating waste heat, dehumidification waste heat, gas combustion waste heat, water heating waste heat, and UHI [K]; diurnal variation of mean and standard variation (band) are shown using data obtained over a two-week period; nighttime is shown with shaded regions; times in Local Standard Time (LST).

speed and turbulent kinetic energy when this heat is released above roof level compared to when it is released near street level. Depending on the urban configuration and amount of urban vegetation the location of waste heat release could affect UHI by even higher magnitudes.

S1.4 Radiation Configuration

The radiation model within VCWG is explored by VCWG simulations under different canyon aspect ratios $\mathrm{H_{avg}/w}$ [-] and different street canyon axis angles θ_{can} [°] with respect to the north axis to investigate the effects on shortwave and longwave fluxes. For exploring the effect of canyon aspect ratio on these fluxes, values of $\mathrm{H_{avg}/w}$=0.8 and 1.6 [-] are used while keeping θ_{can}=0°, while for exploring the effect of street canyon axis angle on these fluxes, values of θ_{can}=0 and 90° with respect to the north axis are used with keeping $\mathrm{H_{avg}/w}$=0.8 [-]. For these explorations VCWG simulations are conducted for two weeks and hourly mean values for radiative fluxes are reported. Here, except for $\mathrm{H_{avg}/w}$ [-] and θ_{can} [°], all other model input parameters are kept the same as the evaluation simulations.

Figure S7 shows the shortwave S [$\mathrm{Wm^{-2}}$] and longwave L [$\mathrm{Wm^{-2}}$] radiative fluxes for different canyon aspect ratios. It can be seen that the net shortwave radiation flux , i.e. incoming $\mathrm{S^{\downarrow}}$ [$\mathrm{Wm^{-2}}$] minus outgoing $\mathrm{S^{\uparrow}}$ [$\mathrm{Wm^{-2}}$] fluxes, by the roof is not affected by the canyon aspect ratio, while the interior surfaces of the urban canyon absorb lower amounts of shortwave

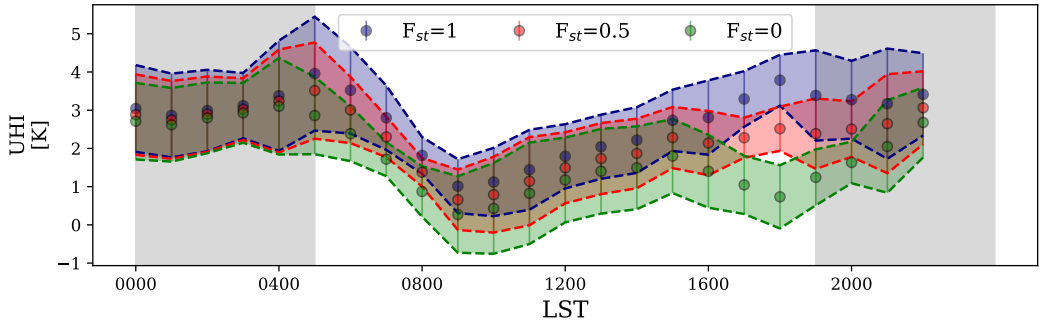

Figure S6. Effect of the location of waste heat release on UHI [K]; diurnal variation of mean and standard deviation (band) are shown using data obtained over a two-week period; nighttime is shown with shaded regions; times in Local Standard Time (LST); blue: all waste heat released at street level (F_{st}=1); red: half of waste heat released at street level (F_{st}=0.5); green: all waste heat released at roof level (F_{st}=0).

radiation fluxes for the higher canyon aspect ratio. This is expected since a higher canyon aspect ratio creates more shading effects on interior canyon surfaces compared to a lower canyon aspect ratio. Focusing on the net shortwave radiation fluxes on the road and tree, it is noted that for the higher aspect ratio canyon the fluxes are more pronounced near noon Local Standard Time (LST), while for the lower aspect ratio canyon the fluxes are pronounced in more hours before and after noon LST. This is expected since a higher aspect ratio canyon creates more shading effects on times before and after noon LST compared to a lower aspect ratio canyon. Focusing on the net longwave radiation fluxes, i.e. incoming $L^{\downarrow}$ [Wm^{-2}] minus outgoing $L^{\uparrow}$ [Wm^{-2}] fluxes, it is noted that the roof is not affected by the canyon aspect ratio, while the road and wall surfaces of the urban canyon lose lesser amounts of longwave radiation for the higher canyon aspect ratio, both during nighttime and daytime. This can be understood as higher longwave radiation trapping by the higher canyon aspect ratio. For trees, it can be seen that during daytime, there can be a net longwave radiation gain (as opposed to loss) due to lower vegetation temperatures compared to the surrounding surfaces.

Figure S8 shows the radiative fluxes for different street canyon axis angles. It can be seen that the shortwave radiation flux absorbed by the roof is not affected by the street canyon axis angle, while the interior surfaces of the urban canyon show different responses to absorbing the shortwave radiation flux given the street canyon axis angle. With θ_{can}=90° the road surface absorbs the shortwave radiation flux over more hours during the day, given that the combined direct and diffuse shortwave fluxes reach the road surface at both low and high solar zenith and azimuth angles from the east and west directions. On the other hand, with θ_{can}=0° the road surface absorbs the shortwave radiation flux in hours around noon LST, given that this flux reaches the road surface effectively only at low solar zenith and azimuth angles from the north direction. With θ_{can}=90° the wall surface absorbs the shortwave radiation flux in most hours during midday, given that this flux reaches the wall surface with multiple combinations of solar zenith and azimuth angles. On the other hand, with θ_{can}=0° the wall surface absorbs little shortwave radiation flux in hours around noon LST, given that this flux does not reach the wall surface when the solar azimuth angle is from the north direction. Focusing on the net longwave radiation flux components, the road exhibits a net longwave radiation loss over more polonged hours of daytime when θ_{can}=90°. The walls exhibit a higher net longwave radiation loss during daytime when θ_{can}=0°. For trees, again, it can be seen that during daytime, there can be a net longwave radiation gain (as opposed to loss) due to lower vegetation temperatures compared to the surrounding surfaces.

S1.5 Seasonal Variations

Performance of VCWG is assessed over different seasons with simulations for Vancouver for an entire year in a period in early 2000s. The model input parameters are chosen to correspond to a plan area density of λ_p=0.39 [-], a ratio of total surface to lot area of about 2.2 [-], and a canyon angle of θ_{can}=−45° (Runnalls and Oke, 2000).

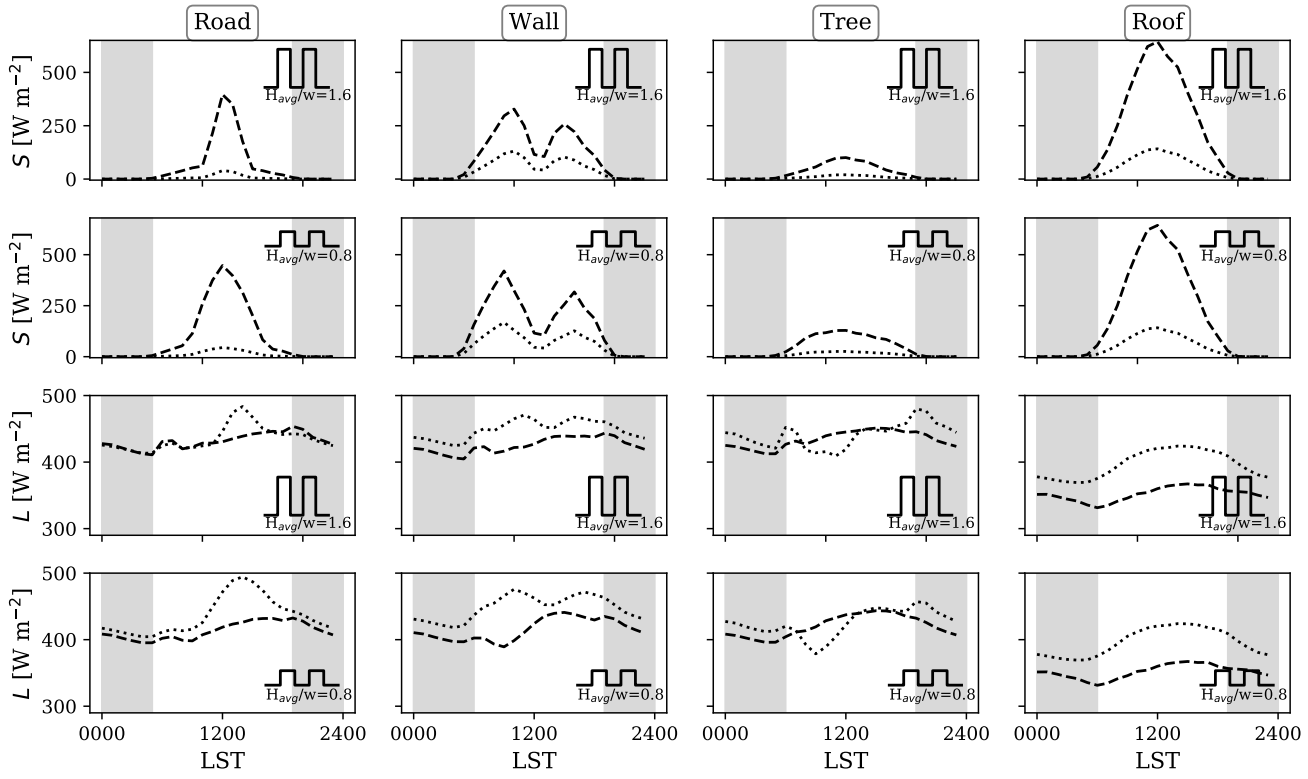

Figure S7. Effect of canyon aspect ratio $\mathrm{H_{avg}/w}$ [-] on hourly mean absolute values of shortwave S [$\mathrm{Wm^{-2}}$] and longwave L [$\mathrm{Wm^{-2}}$] radiation fluxes; incoming fluxes ($\mathrm{S^{\downarrow}}$ and $\mathrm{L^{\downarrow}}$ [$\mathrm{Wm^{-2}}$]) shown using dashed lines; outgoing fluxes ($\mathrm{S^{\uparrow}}$ and $\mathrm{L^{\uparrow}}$ [$\mathrm{Wm^{-2}}$]) shown using dotted lines; diurnal variation of mean is shown using data obtained over a two-week period; nighttime is shown with shaded regions; times in Local Standard Time (LST).

Figure S9 shows the VCWG results for the hourly mean values of UHI [K] in each month of the year in Vancouver, Canada. It can be noted that in general early daytime UHI [K] values are lower than nighttime values, as expected. Also the greatest UHI [K] values are noted to occur in August and September. The seasonal variation of UHI [K] as predicted by VCWG is in agreement with a similar map reported by Oke et al. (2017).

Figure S10 shows the profiles of potential temperature, horizontal wind speed, specific humidity, and turbulent kinetic energy during nighttime (averaged at 0200 LST) and daytime (averaged at 1400 LST) in different seasons for the Vancouver simulation. It is notable that the potential temperature and specific humidity profiles reflect the seasonal patterns (low values in the winter and high values in the summer). Wind speed and turbulent kinetic energy profiles do not reveal notable seasonal variations.

S1.6 Other Climates

The VCWG is further explored by predicting UHI [K] in different cities with different climate zones including Buenos Aires in February 1996, a city in the southern hemisphere with a hot and humid climate, Vancouver in September 2011, representing a moderate oceanic climate, Osaka in August 1989, with a subtropical climate, and Copenhagen in June 1999, representing a cold and temperate climate. All simulations are conducted for two weeks and then the hourly mean and standard deviations of

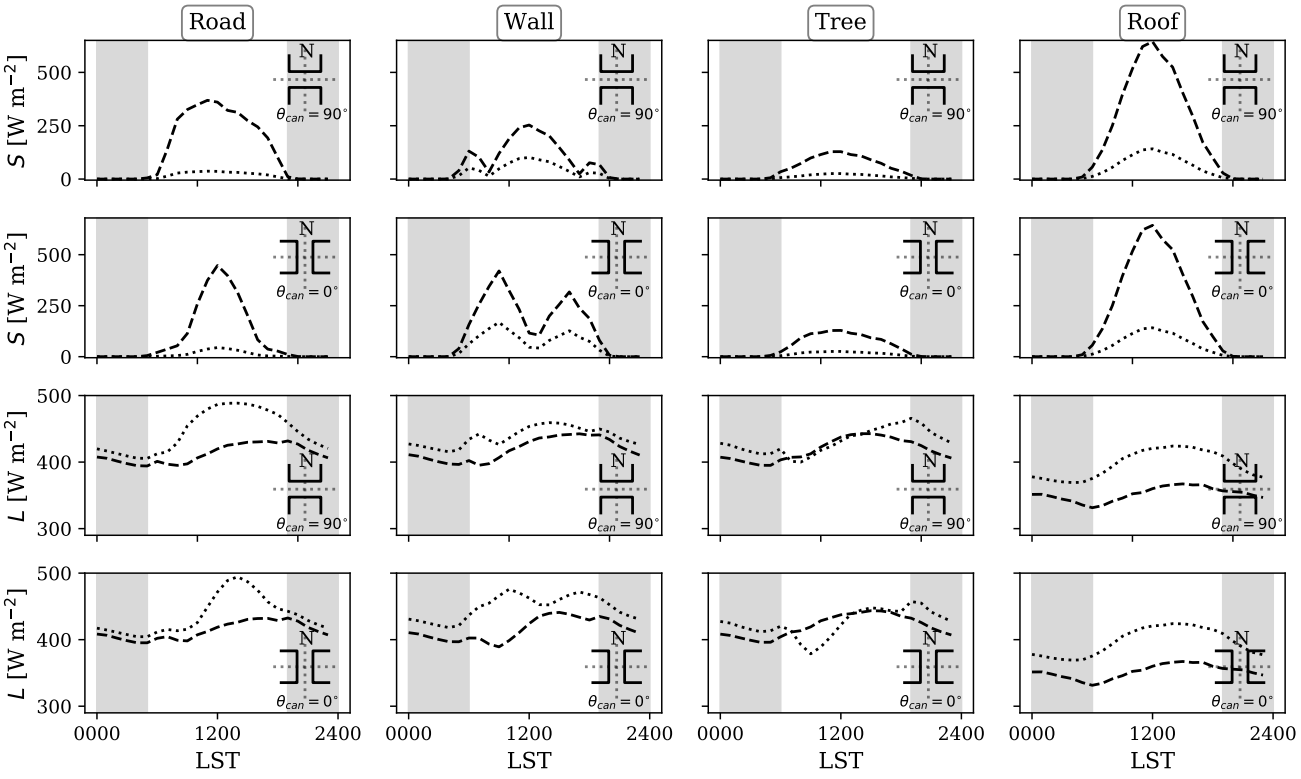

Figure S8. Effect of street canyon axis angle θ_{can} [°] on hourly mean absolute values of shortwave S [Wm^{-2}] and longwave L [Wm^{-2}] radiation fluxes; incoming fluxes ($\mathrm{S}^{\downarrow}$ and $\mathrm{L}^{\downarrow}$ [Wm^{-2}]) shown using dashed lines; outgoing fluxes ($\mathrm{S}^{\uparrow}$ and $\mathrm{L}^{\uparrow}$ [Wm^{-2}]) shown using dotted lines; diurnal variation of mean is shown using data obtained over a two-week period; nighttime is shown with shaded regions; times in Local Standard Time (LST).

UHI are calculated (see Fig. S11). In all simulations it is assumed that all of the building waste heat is released at roof level, i.e. $F_{st} = 0$.

For Buenos Aires, VCWG predicts UHI values of $+2.5$, $+0.1$, -0.5, and $+2.4$ K at 0300, 0900, 1500, and 2100 LST, respectively. The observed values for the same hours were $+2.1$, $+1$, $+0.1$, and $+1.5$, respectively. On average, the VCWG predictions of UHI ($+1.1$ K) are in good agreement with those of the observation ($+1.2$ K) (Camilloni and Barrucand, 2012). In case of Vancouver, VCWG predicts maximum and minimum values of UHI equal to $+2.7$ and $+0.1$ K, respectively. The observed values for the maximum and minimum UHI were $+3.8$ and -1 K, respectively (Runnalls and Oke, 2000), in reasonable agreement with the predictions. Case studies in Japan have reportedly obtained urban warming in large and developed cities such as Osaka, which is the interest in this study. This effect is also predicted by VCWG that shows a monthly-averaged UHI of $+1.78$ K, which is consistent with a monthly-average of $+2.2$ K simulated using meso-scale modelling (Kusaka et al., 2012). UHI [K] in Copenhagen is reported to change between $+0.25$ and $+1.5$ K depending on the wind speed (Mahura et al., 2009), which agrees reasonably well with the VCWG predictions of UHI [K] varying from a -0.4 K to $+1.9$ K.

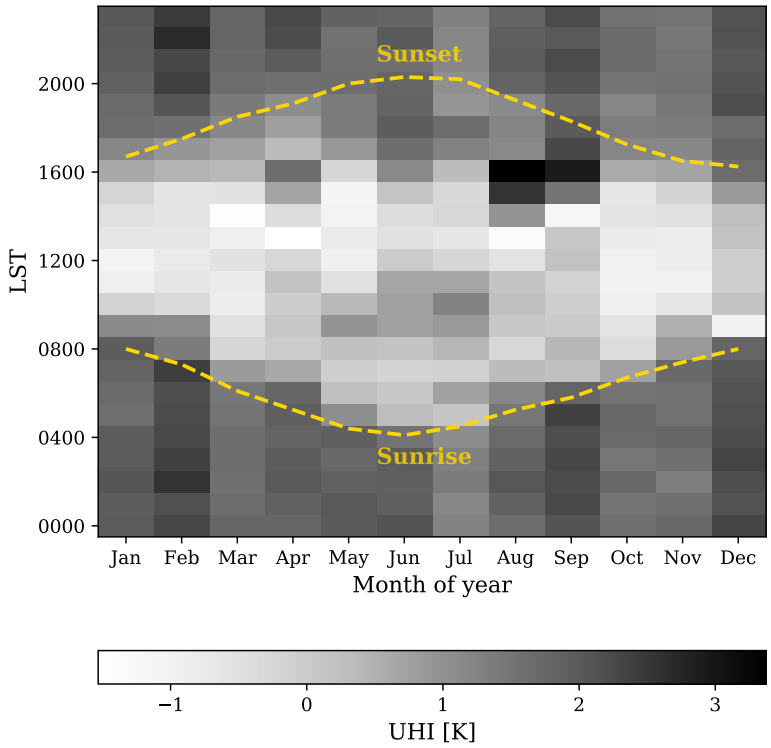

Figure S9. Hourly mean values of UHI [K] in each month in Vancouver, Canada, as predicted by VCWG; sunrise and sunset times are denoted by dashed lines; times in Local Standard Time (LST).

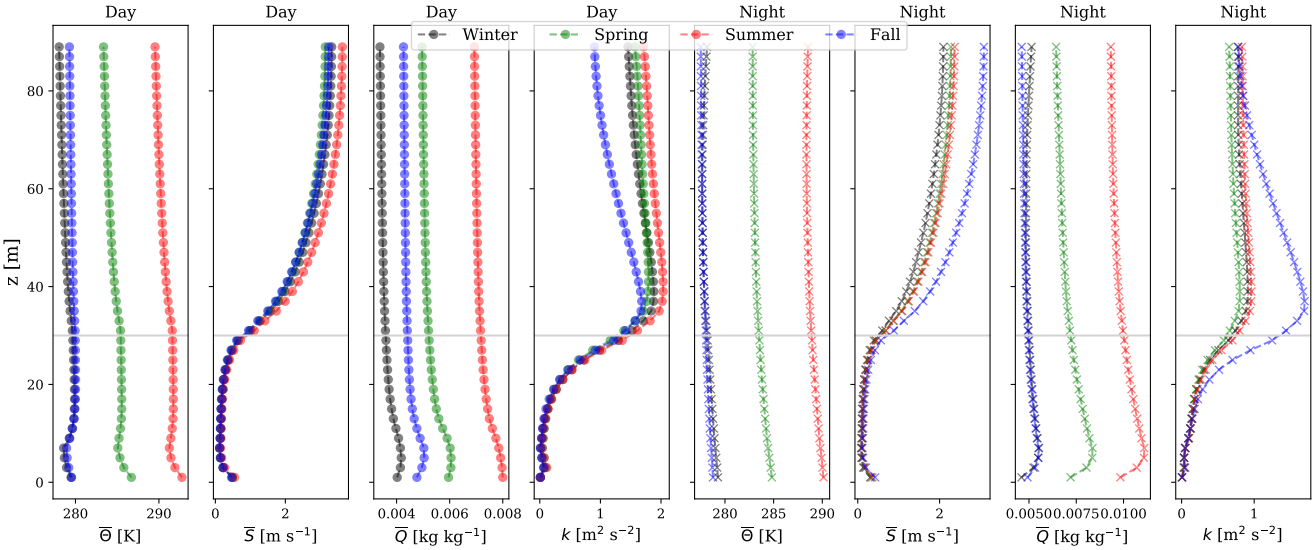

Figure S10. Profiles of potential temperature, horizontal wind speed, specific humidity, and turbulent kinetic energy during nighttime (averaged at 0200 LST) and daytime (averaged at 1400 LST) in different seasons; black: winter, green: spring , red: summer, and blue: fall; building height shown with grey line; times in Local Standard Time (LST).

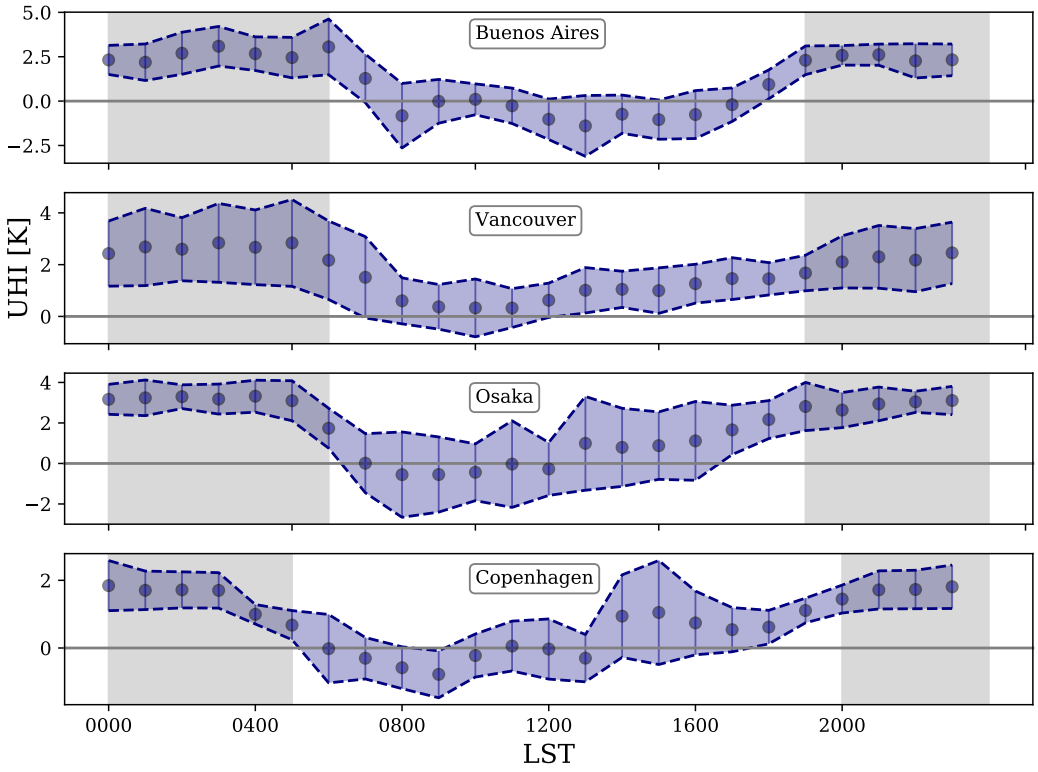

Figure S11. Diurnal variation of the UHI [K], as predicted by VCWG, in Buenos Aires, Vancouver, Osaka, and Copenhagen; diurnal variation of mean and standard deviation (band) are shown using data obtained over a two-week period; nighttime is shown with shaded regions; times in Local Standard Time (LST).

References

Akbari, H., Pomerantz, M., and Taha, H.: Cool surfaces and shade trees to reduce energy use and improve air quality in urban areas, Sol. Energy, 70, 295–310, https://doi.org/10.1016/S0038-092X(00)00089-X, 2001.

Bueno, B., Norford, L. K., Hidalgo, J., and Pigeon, G.: The urban weather generator, J. Build. Perf. Simulat., 6, 269–281, https://doi.org/10.1080/19401493.2012.718797, 2012.

Camilloni, I. and Barrucand, M.: Temporal variability of the Buenos Aires, Argentina, urban heat island, Theor. Appl. Climatol., 107, 47–58, https://doi.org/10.1007/s00704-011-0459-z, 2012.

Coutts, A. M., Beringer, J., and Tapper, N. J.: Impact of increasing urban density on local climate: spatial and temporal variations in the surface energy balance in Melbourne, Australia, J. Appl. Meteorol. Clim., 46, 477–493, https://doi.org/10.1175/JAM2462.1, 2007.

Emmanuel, R. and Steemers, K.: Connecting the realms of urban form, density and microclimate, Build. Res. Inf., 46, 804–808, https://doi.org/10.1080/09613218.2018.1507078, 2018.

Giometto, M. G., Christen, A., Egli, P. E., Schmid, M. F., Tooke, R., Coops, N. C., and Parlange, M. B.: Effects of trees on mean wind, turbulence and momentum exchange within and above a real urban environment, Adv. Water Resour., 106, 154–168, https://doi.org/10.1016/j.advwatres.2017.06.018, 2017.

Krayenhoff, E. S.: A multi-layer urban canopy model for neighbourhoods with trees, Ph.D. thesis, University of British Columbia, Vancouver, https://doi.org/10.14288/1.0167084, 2014.

Krayenhoff, E. S., Santiago, J.-L., Martilli, A., Christen, A., and Oke, T. R.: Parametrization of drag and turbulence for urban neighbourhoods with trees, Bound.-Lay. Meteorol., 156, 157–189, https://doi.org/10.1007/s10546-015-0028-6, 2015.

Kusaka, H., Hara, M., and Takane, Y.: Urban climate projection by the WRF model at 3-km horizontal grid increment: dynamical downscaling and predicting heat stress in the 2070's August for Tokyo, Osaka, and Nagoya metropolises, J. Meteorol. Soc. Jpn. Ser. II, 90, 47–63, https://doi.org/10.2151/jmsj.2012-B04, 2012.

Loughner, C. P., Allen, D. J., Zhang, D.-L., Pickering, K. E., Dickerson, R. R., and Landry, L.: Roles of urban tree canopy and buildings in urban heat island effects: parameterization and preliminary results, J. Appl. Meteorol. Clim., 51, 1775–1793, https://doi.org/10.1175/JAMC-D-11-0228.1, 2012.

Mahura, A., Baklanov, A., Petersen, C., Nielsen, N. W., and Amstrup, B.: Verification and case studies for urban effects in HIRLAM numerical weather forecasting, in: Meteorological and Air Quality Models for Urban Areas, pp. 143–150, Springer, Berlin, https://doi.org/10.1007/978-3-642-00298-4_14, 2009.

Oke, T. R., Mills, G., Christen, A., and Voogt, J. A.: Urban Climates, Cambridge University Press, London, https://doi.org/10.1017/9781139016476, 2017.

Redon, E. C., Lemonsu, A., Masson, V., Morille, B., and Musy, M.: Implementation of street trees within the solar radiative exchange parameterization of TEB in SURFEX v8.0, Geosci. Model Dev., 10, 385–411, https://doi.org/10.5194/gmd-10-385-2017, 2017.

Runnalls, K. E. and Oke, T. R.: Dynamics and controls of the near-surface heat island of Vancouver, British Columbia, Physical Geography, 21, 283–304, https://doi.org/10.1080/02723646.2000.10642711, 2000.

Santiago, J. L., Krayenhoff, E. S., and Martilli, A.: Flow simulations for simplified urban configurations with microscale distributions of surface thermal forcing, Urban Climate, 9, 115–133, https://doi.org/10.1016/j.uclim.2014.07.008, 2014.

Souch, C. A. and Souch, C.: The effect of trees on summertime below canopy urban climates: a case study Bloomington, Indiana, J. Arboriculture, 19, 303–312, 1993.

Wong, M. S., Nichol, J. E., To, P. H., and Wang, J.: A simple method for designation of urban ventilation corridors and its application to urban heat island analysis, Build. Environ., 45, 1880–1889, https://doi.org/10.1016/j.buildenv.2010.02.019, 2010.

Yuan, C., Norford, L. K., and Ng, E.: A semi-empirical model for the effect of trees on the urban wind environment, Landscape Urban Plan., 168, 84–93, https://doi.org/10.1016/j.landurbplan.2017.09.029, 2017.

Zajic, D., Fernando, H. J. S., Calhoun, R., Princevac, M., Brown, M. J., and Pardyjak, E. R.: Flow and turbulence in an urban canyon, J. Appl. Meteorol. Clim., 50, 203–223, https://doi.org/10.1175/2010JAMC2525.1, 2011.